

# Tailoring weld geometry during keyhole mode laser welding using a genetic algorithm and a heat transfer model

R Rai and T DebRoy

Department of Materials Science and Engineering, The Pennsylvania State University, University Park, PA 16802, USA

Received 10 November 2005, in final form 31 January 2006

Published 3 March 2006

Online at [stacks.iop.org/JPhysD/39/1257](http://stacks.iop.org/JPhysD/39/1257)

## Abstract

Tailoring of weld attributes based on scientific principles remains an important goal in welding research. The current generation of unidirectional laser keyhole models cannot determine sets of welding variables that can lead to a particular weld attribute such as specific weld geometry. Here we show how a computational heat transfer model of keyhole mode laser welding can be restructured for systematic tailoring of weld attributes based on scientific principles. Furthermore, the model presented here can calculate multiple sets of laser welding variables, i.e. laser power, welding speed and beam defocus, with each set leading to the same weld pool geometry. Many sets of welding variables were obtained via a global search using a real number-based genetic algorithm, which was combined with a numerical heat transfer model of keyhole laser welding. The reliability of the numerical heat transfer calculations was significantly improved by optimizing values of the uncertain input parameters from a limited volume of experimental data. The computational procedure was applied to the keyhole mode laser welding of the 5182 Al–Mg alloy to calculate various sets of welding variables to achieve a specified weld geometry. The calculated welding parameter sets showed wide variations of the values of welding parameters, but each set resulted in a similar fusion zone geometry. The effectiveness of the computational procedure was examined by comparing the computed weld geometry for each set of welding parameters with the corresponding experimental geometry. The results provide hope that systematic tailoring of weld attributes via multiple pathways, each representing alternative welding parameter sets, is attainable based on scientific principles.

## 1. Introduction

During laser welding, the high power density of the laser beam results in rapid melting and superheating of the molten metal. Within the weld pool, the liquid metal undergoes vigorous circulation driven by Marangoni convection and heat transfer occurs mainly by convection [1–7]. When the power density exceeds a critical value, a vapour cavity or keyhole forms inside the molten metal. Laser welding is often conducted in the keyhole mode for welding of thick plates. Several models have been proposed [8–22] to understand temperature fields, weld geometry and keyhole profiles. For example, Swift-Hook and Gick [8] calculated weld width by treating

the laser beam as a moving line heat source. Andrews and Atthey [9] modelled the keyhole geometry based on the energy balance on the keyhole wall. Klemens [10] calculated the keyhole shape considering vapour pressure within the keyhole, surface tension of liquid metal and the pressure in the molten metal. Mazumder and Steen [11] modelled temperature field by assuming complete laser absorption on the surface where the temperature exceeded the boiling point. Dowden *et al* [12,13] computed temperature field and weld pool geometry by assuming a cylindrical keyhole of a known radius. The keyhole surface was assumed to be at the boiling point. Kross *et al* [16] calculated the keyhole geometry considering vaporization from the keyhole surface, surface tension, pressures in the

melt and heat conduction into the work piece. Sudnik *et al* [17] calculated the energy absorption efficiency from the fundamental principles of radiation absorption and energy loss. Metzbowler [18] estimated the temperature field in the work-piece considering laser power loss due to evaporation. *In situ* x-ray transmission imaging studies [19,20] established that the keyhole was not symmetrical with respect to the beam axis for high speed welding. It was observed that the front keyhole wall had a larger angle of inclination than the rear wall. Arata *et al* [20] suggested that the bent keyhole shape was caused by inertia and the ‘wall focusing’ effect that resulted in the difference in energy absorption in different parts of the keyhole wall. Kaplan [21] predicted the asymmetry of the keyhole by considering the different rates of heat transfer at different regions of the keyhole. Zhao and DebRoy [22] applied a heat transfer model to determine the keyhole geometry and temperature profiles in aluminium alloy laser welds in three dimensions. Although a critical review of the previous work indicates that the models have provided significant insight on the welding process and welded materials, they are not widely used in designing and manufacturing today.

Two main difficulties have to be overcome for the widespread use of the models described above. First, the predictions of temperature fields and weld geometry do not always agree with the experimental results because some model input variables such as the laser beam absorptivity cannot be prescribed from fundamental principles. Second, the current generation unidirectional heat transfer models are designed to calculate temperature fields from welding conditions, i.e. welding speed, laser power, absorption coefficient, laser beam radius, beam defocus. However, what is often needed and not currently attainable is to determine the welding variables required to achieve a given weld attribute such as the weld geometry. Finally, the laser welding system is highly complex and involves non-linear interaction of several welding variables. As a result, a particular weld attribute such as the geometry can be obtained via multiple paths, i.e. through the use of various sets of welding variables. The available numerical heat transfer models cannot determine alternative pathways to achieve a target weld attribute.

Here we show that by combining a numerical heat transfer model with a suitable optimization algorithm, these major problems can be solved. First, the reliability of the calculated results can be improved by estimating uncertain input parameters, such as the laser beam absorption coefficient and beam radius at focus, from a limited volume of experimental data. By coupling a genetic algorithm (GA)-based optimization method [23, 24] with a three-dimensional (3D) heat transfer model [25], the optimized values of these uncertain parameters can be determined so that the computed weld geometry agrees well with the experimental data. Second, the GA can systematically search for multiple solution sets of welding variables [25–27], welding speed, laser power and beam defocusing, each of which can result in a specific weld geometry. Since the search involves a well-tested forward heat transfer model for keyhole mode welding, the estimation of uncertain parameters and multiple sets of welding variables complies with the phenomenological laws of welding

**Table 1.** Data used in the calculations.

Physical Property	Value
Boiling point (K)	1930
Solidus temperature (K)	850
Density ( $\text{kg m}^{-3}$ )	2300
Specific heat ( $\text{J kg}^{-1} \text{K}^{-1}$ )	1200
Thermal conductivity ( $\text{W m}^{-1} \text{K}^{-1}$ )	108
Beam diameter at the end of the focusing lens (mm)	28
Focal length of lens (mm)	78
Heat of evaporation of Al ( $\text{J kg}^{-1}$ )	$1.078 \times 10^7$
Heat of evaporation of Mg ( $\text{J kg}^{-1}$ )	$5.253 \times 10^6$
Inverse Bremsstrahlung absorption coefficient ( $\text{m}^{-1}$ )	100
Heat transfer coefficient ( $\text{W m}^{-2} \text{K}^{-1}$ )	15

physics. Various sets of welding variables needed to achieve a specified weld geometry during keyhole mode laser welding of the 5182 Al–Mg alloy were calculated. The calculated welding parameter sets showed wide variations of the values of welding parameters. However, the fusion zone geometry computed from each of the diverse set of input parameters were very similar, and these were compared with the specified weld geometry.

## 2. The mathematical model

### 2.1. Modelling of heat transfer during keyhole mode laser welding

A 3D heat transfer model [21, 22] is used as the main computational engine for the calculation of temperature fields from a set of specified welding conditions and materials properties. The main assumptions of the model are the following. The temperature on the keyhole wall is taken to be the boiling point of the alloy. Since the keyhole is exposed to the atmosphere, the equilibrium pressures of all the alloying elements add up to one atmosphere. Furthermore, since the orientation of the keyhole is almost vertical, and the temperature everywhere at the keyhole wall is the boiling point of the alloy, the heat transfer takes place mainly along the horizontal plane. A constant laser beam absorption coefficient, independent of location, is assumed for the plasma in the keyhole and the laser beam absorption at the keyhole wall.

The model calculates weld geometry based on several parameters which include material properties, welding process parameters and geometrical parameters. Values used for the input parameters are listed in table 1.

The 2D temperature field in an infinite plate can be calculated considering the conduction heat from the keyhole wall into the plate as [30]

$$T(r, \varphi) = T_a + \frac{P'}{2\pi\lambda} K_0(\Omega r) e^{-\Omega r \cos \varphi}, \quad (1)$$

where  $(r, \varphi)$  designates the location in the plate with the line source as the origin,  $T_a$  is the ambient temperature,  $P'$  is the power per unit depth,  $\lambda$  is the thermal conductivity,  $K_0(\cdot)$  is the solution of the second kind and the zero-order modified Bessel function and,  $\Omega = \nu/(2\kappa)$ , where  $\nu$  is the welding speed and  $\kappa$  is the thermal diffusivity.

**Table 2.** Welding variables and experimentally measured weld pool depth and width [35].

Data set	Power (W)	Welding speed (mm s <sup>-1</sup> )	Defocus (mm)	Experimental value	
				Weld pool depth (mm)	Weld pool width (mm)
(a)	2600	63.5	0.0	1	2.35 1.67
(b)	2600	74.1	0.0	1	2.27 1.83
(c)	2600	84.7	0.0	1	1.96 1.23
(d)	2600	93.5	0.0	1	1.73 0.73
(e)	2600	105.8	0.0	1	1.63 0.56

The radial heat flux conducted into the keyhole wall,  $I_c$ , can be obtained from the relation

$$I_c(r, \varphi) = -\lambda \frac{\partial T(r, \varphi)}{\partial r}. \quad (2)$$

The locally absorbed beam energy flux,  $I_a$ , on the keyhole wall taking into account the absorption by the work-piece during multiple reflections and the plasma absorption is calculated as [21]

$$I_a = e^{-\beta l} (1 - (1 - \alpha)^{\pi/(4\theta)}) I_0, \quad (3)$$

where  $\beta$  is the inverse Bremsstrahlung absorption coefficient of plasma,  $l$  is the average path of the laser beam in the plasma before it reaches the keyhole wall,  $\alpha$  is the absorption coefficient of the work-piece,  $\theta$  is the average angle between the keyhole wall and the initial incident beam axis and  $I_0$  is the local incident beam intensity.

The evaporative heat flux,  $I_v$ , on the keyhole wall is given as

$$I_v = \sum_{i=1}^n J_i \Delta H_i, \quad (4)$$

where  $n$  is the total number of alloying elements in the alloy,  $\Delta H_i$  is the heat of evaporation of element  $i$  and  $J_i$  is the evaporation flux of element  $i$  given by the modified Langmuir equation [31–33]:

$$J_i = \frac{a_i P_i^0}{7.5} \sqrt{\frac{M_i}{2\pi RT_b}}, \quad (5)$$

where  $a_i$  is the activity of element  $i$ ,  $P_i^0$  is the equilibrium vapour pressure of element  $i$  over pure liquid at the boiling point  $T_b$  and  $M_i$  is the molecular weight of element  $i$ . Factor 7.5 is used to account for the diminished evaporation rate at one atmosphere pressure compared to the vaporization rate in vacuum and is based on previous experimental results [32,33].

A simple heat flux balance on the keyhole wall gives the following relation for the local keyhole wall angle,  $\theta$ :

$$\tan(\theta) = \frac{I_c}{I_a - I_v}. \quad (6)$$

The keyhole model solves these equations to calculate the temperature distribution in the work-piece from the top surface of the sample up to the bottom of the keyhole. To calculate the temperature profile below the keyhole and hence to calculate the total weld pool depth, the model is combined with another computer code which solves the following heat conduction equation:

$$\frac{\partial^2 T}{\partial x^2} + \frac{\partial^2 T}{\partial y^2} + \frac{\partial^2 T}{\partial z^2} - \frac{\nu}{\kappa} \frac{\partial T}{\partial x} = 0, \quad (7)$$

where  $\nu$  is the welding speed and  $\kappa$  is the thermal diffusivity of the work-piece. The other boundary conditions are as follows.

The boundary condition for the bottom surface is given by

$$J(x, y, z)|_{z=\max} = h[T_a - T(x, y, z)|_{z=\max}], \quad (8)$$

where  $J(x, y, z)$  is the heat flux,  $h$  is the heat transfer coefficient,  $T_a$  is the ambient temperature and  $T(x, y, z)$  is the local temperature.

The temperatures at all other surfaces are assumed to be ambient temperature since the surfaces are far away from the heat source. The numerical model for the solution of the above equations, henceforth referred to as the forward numerical model, gives the complete temperature profile in the work-piece.

## 2.2. GA as an optimization model

The first step in the computational procedure is to optimize the values of the uncertain parameters in the model, namely, the radius at focus ( $r$ ) and the laser beam absorption coefficient ( $\alpha$ ). A population of randomly generated sets of uncertain parameters is initially formed by the GA [28,29,34]. Calculations of the forward numerical model are done for each of the sets of uncertain parameters, for each of the welding conditions in the experimental data set, and the weld pool depth and width are obtained. The experimental data set used for this study, consisting of five welding conditions and the corresponding weld pool dimensions, i.e. depth and width, are shown in table 2. The deviation of computed depth and width from the corresponding experimentally observed results can be quantified by the following objective function:

$$O1(f) = \sum_{k=1}^5 \left[ \left| \frac{d^c}{d^e} - 1 \right|_k + \left| \frac{w_t^c}{w_t^e} - 1 \right|_k + \left| \frac{w_b^c}{w_b^e} - 1 \right|_k \right], \quad (9)$$

where  $k$  designates the specific set of welding conditions given in table 2,  $d^c$ ,  $w_t^c$  and  $w_b^c$  are the computed weld pool depth, width at the top of the work-piece and width at the bottom of the work-piece, respectively, and  $d^e$ ,  $w_t^e$ , and  $w_b^e$  are the corresponding experimental weld pool depth, width at the top of the work-piece and width at the bottom of the work-piece for these sets of welding conditions. Note that for each of the five welding conditions the experimental weld depth was equal to the work-piece thickness. Two values of width have been specified for the weld pool cross-section, i.e. at the top and bottom of the work-piece to ensure a better correspondence between a low objective function  $O1(f)$  and a good agreement between the calculated and the experimental weld pool geometry.

The objective function  $O1(f)$  depends on the beam radius at focus  $r$  and the absorption coefficient  $\alpha$ :

$$O1(f) = f\left(\frac{r}{r^0}, \alpha\right), \quad (10)$$

where  $r^0 = 0.3$  mm is a reference value of the radius of the beam experimentally measured at the focal point. The random values of  $r$  are generated by the following scheme. The value of the relative error  $e$  in the beam radius is randomly generated within a negative lower limit and a positive upper limit. The upper and lower limits are the specified maximum positive and negative errors, respectively, in the measurement of radius. The relative error in the beam radius,  $e$ , can be either positive or negative. The value of  $r$  is then calculated as

$$r = (1 + e)r^0. \quad (11)$$

The values of the absorption coefficient are also randomly generated within an upper and a lower limit. A systematic global search is then undertaken by the GA to find the set of uncertain parameters which result in the least value of the objective function, i.e. which give weld pool depth and width values very close to the experimental values. The effectiveness of the search for optimized values of the two parameters is enhanced by using dimensionless values of radius which is comparable in magnitude to the absorption coefficient. The sets of unknown input parameters, commonly referred to as population in GA, change with every iteration following the rules of GA [23, 24, 28, 29]. The GA used in the present study is a parent-centric recombination (PCX) operator-based generalized generation gap (G3) model [28, 29]. The specific application for using this model for optimizing sets of unknown input parameters is explained in the appendix.

After obtaining the optimized values of uncertain parameters using GA, the next step is to search for multiple pathways or different sets of welding variables, i.e. laser power, welding speed and beam defocusing to obtain a pre-defined specific weld geometry. An initial population of randomly selected welding variables is formed by the GA. For each set of the welding variables, the forward numerical model calculates the weld pool dimensions, i.e. depth and width at top and bottom of the work-piece. Not all sets of welding variables result in the desired weld pool geometry. The deviation between the weld pool geometry for any set of welding variables and the target geometry is obtained as

$$O2(f) = \left| \frac{d^c}{d^e} - 1 \right| + \left| \frac{w_t^c}{w_t^e} - 1 \right| + \left| \frac{w_b^c}{w_b^e} - 1 \right|, \quad (12)$$

where  $d^c$ ,  $w_t^c$  and  $w_b^c$  are the computed weld pool depth, width at the top of the work-piece, and width at the bottom of the work-piece, respectively, and  $d^e$ ,  $w_t^e$ , and  $w_b^e$  are the corresponding experimental weld pool depth, width at the top of the work-piece and width at the bottom of the work-piece for the target geometry chosen for the study. The objective function depends on the three welding variables: laser power  $P$ , welding speed  $v$  and beam defocusing  $\delta$ .

$$O2(f) = O2\left(\frac{P}{P^0}, \frac{v}{v^0}, \frac{\delta}{\delta^0}\right), \quad (13)$$

where  $P^0$ ,  $v^0$  and  $\delta^0$  are the reference values of the variables that represent the order of magnitude of the respective variables. The non-dimensional values of different welding variables are comparable in magnitude. Thus, the importance of each welding variable is preserved by their non-dimensional values. The actual values of the welding variables are calculated by multiplying the non-dimensional value with the corresponding reference value. The GA then systematically searches for sets of welding variables that produce weld dimensions that are close to the target dimensions. The search involves improvement in the values of the GA population with iterations following certain laws of the GA [23, 24, 28, 29]. The specific application for using this model for obtaining multiple sets of welding variables is similar to the one described in the appendix.

### 3. Results and discussion

#### 3.1. Improving reliability of calculated results

Since the model is based on well-tested equations of heat transfer the mismatch between the computed and the experimental results may be attributed primarily to uncertainties in some of the input parameters. Values of beam radius at focus and the absorption coefficient were identified as the most important uncertain parameters and their values were estimated from a limited volume of the experimental data. The data used for the calculations are listed in table 2. The absorption coefficient for clean flat surfaces can be estimated from the following relation based on the assumption that energy absorption is due to a photon–electron interaction [36]:

$$\alpha = 0.365 \left(\frac{\rho}{\lambda}\right)^{1/2} - 0.0667 \left(\frac{\rho}{\lambda}\right) + 0.006 \left(\frac{\rho}{\lambda}\right)^{3/2}, \quad (14)$$

where  $\rho$  is the electrical resistivity (ohm-centimetres) of the liquid metal at the boiling point and  $\lambda$  is the wavelength (centimetres) of the incident laser beam. However, the estimated absorption coefficient may differ from the actual value owing to surface imperfections. There can also be significant errors in the measured value of the beam radius measured at the focal point. Using the GA, the value of radius was estimated to be 0.232 mm and the value of absorption coefficient was estimated as 0.096. The optimized values of uncertain parameters were used to calculate the weld geometry for the five sets of welding conditions listed in table 2. Equilibrium solidus temperature of the 5182 Al alloy marks the calculated weld pool boundary. Figures 1(a)–(e) show reasonable agreement between the calculated and the experimentally measured weld pool dimensions indicating that the computed values of the laser beam absorption coefficient and the beam radius are appropriate.

Figure 2 shows the calculated 3D temperature fields in the work-piece for the welding conditions corresponding to data set five listed in table 2. Welding is in the positive  $x$  direction. The contour for the boiling point of the alloy (=1930 K) defines the keyhole boundary whereas the region between the boiling point and solidus temperature (=850 K) indicates the weld pool. As seen in figure 2, the front wall of the keyhole is more inclined than the rear wall. At the front of the weld, there is a steeper temperature gradient due to the cold metal

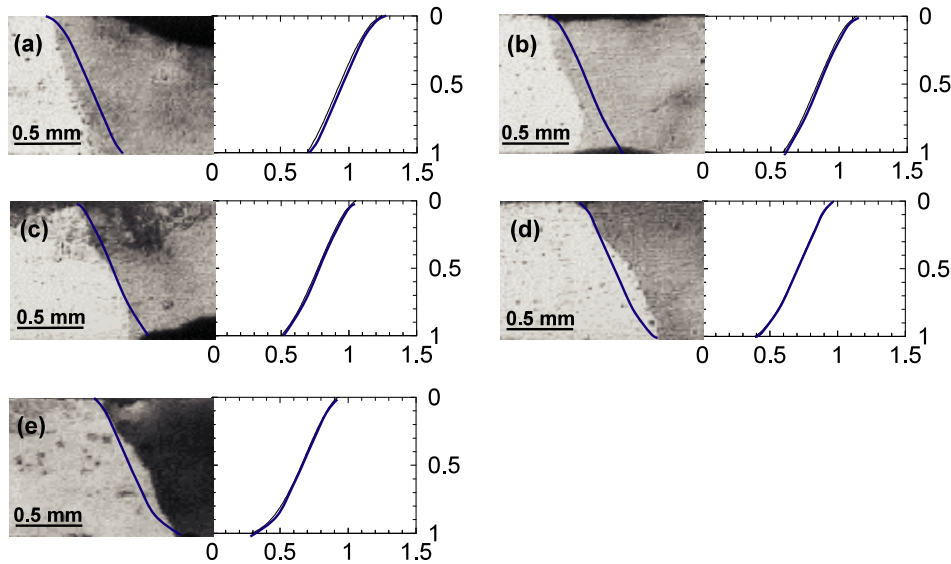


**Figure 1.** Experimental and calculated weld pool dimensions for the five sets of welding conditions given in table 2, i.e. 2600 W power, 0 mm defocus and (a)  $63.5 \text{ mm s}^{-1}$ , (b)  $74.1 \text{ mm s}^{-1}$ , (c)  $84.7 \text{ mm s}^{-1}$ , (d)  $93.5 \text{ mm s}^{-1}$  and (e)  $105.8 \text{ mm s}^{-1}$ . The solid lines are the calculated weld pool boundaries.

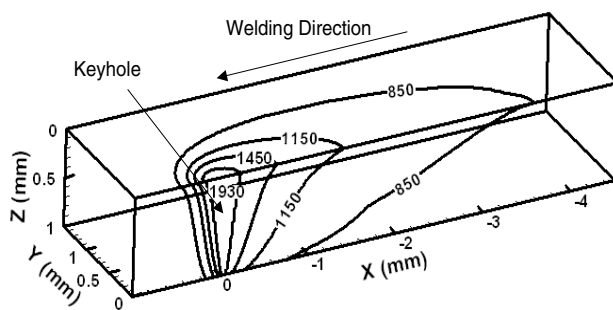


**Figure 2.** Computed temperature fields: 5182 Al alloy, power: 2600 W, speed:  $106 \text{ mm s}^{-1}$ , defocus: 0 mm. Temperatures on isotherms are in kelvin

ahead. Thus more heat is conducted into the plate at the front than at the rear. Thus, according to equation (6), the front wall of the keyhole should be more inclined than the rear wall. This asymmetry of the keyhole profile was also reported in independent investigations [21, 22].

### 3.2. Finding multiple sets of welding process variables

The first step towards obtaining multiple solution sets of welding variables for a specified weld geometry is to define a desired weld geometry. Weld geometry has been defined with the help of three parameters as described previously, i.e. depth, width at the top of the work-piece and width at the bottom of the work-piece. For this study, weld geometry corresponding to experimental data set 3 in table 2 was chosen as the target weld geometry. Thus, one or more solutions in the GA population with an acceptable low objective function value is likely to have values of welding variables very close to the corresponding welding variables of data set 3.

Once the target geometry was identified, the GA was used to calculate multiple sets of welding variables, i.e. laser power, welding speed and beam defocusing which would result in the desired weld geometry. The calculation starts

by randomly generating values of the welding variables within their specified ranges to ensure a diverse initial population. The goal was to minimize the chances of the population becoming similar without much improvement in the objective function value, and/or in case of a requirement of multiple solutions, most of the low objective function members have almost similar values. For this study, a GA population size of 200 was chosen. This number of variable sets was chosen based on how the population size influenced the effectiveness of the GA using standard test functions [28, 29] and the spread of the GA variables for this problem.

The initial GA population, i.e. sets of laser power, welding speed and beam defocus are shown in figure 3. The values of input power were chosen in the range of 1500 to 3500 W, welding speed in the range of 45 to  $210 \text{ mm s}^{-1}$  and beam defocus in the range of  $-1.5$  to  $+1.5$  mm. The variable sets were then improved iteratively. Iterations were stopped when the objective function values for a sufficient percentage of the GA population were below a prescribed limit. The objective function values for the initial GA population set, shown in figure 3(a), are plotted in figure 3(b). For several sets of welding variables the objective function value is very low when compared with the general population. This indicates a possibility of finding solution sets near these 'peaks' with sufficiently low objective function values.

Figure 4(a) shows that the average value of the objective function decreases with iterations. However, the figure also shows that the average objective function sometimes changes abruptly with iterations. For example, a sudden increase in the objective function value was observed after 75 iterations. Sometimes several individuals form a cluster around a single solution during iterations. To promote diversity, the crowding was reduced every twenty five iterations by replacing all individuals in the cluster, except the best individual, with randomly generated individuals. The new members affected the average fitness values significantly after 75 iterations as seen in figure 4(a). The objective function for the best member

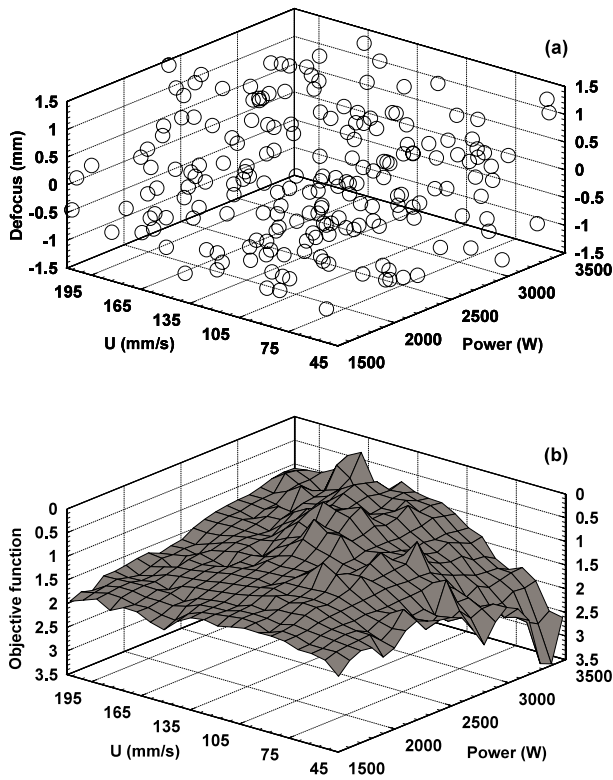


**Figure 3.** Initial population of randomly chosen values of welding variable sets and their objective function values. (a) A large space of variables was searched to find optimum solutions and (b) low values of objective function for several sets of welding variables suggest presence of multiple optimal solutions.

of the population also decreased with iterations as shown in figure 4(b) although not continuously. The creation of new members clearly affects the minimum values of the objective function with iterations and the variation is not continuous because of the uncertain nature of the fitness changes with iterations. Figure 4(c) shows almost a gradual increase in the number of qualified low objective function individuals with iterations. Abrupt changes in the behaviour occur when individuals in a cluster are deliberately replaced by randomly selected individuals to reduce the elite preserving nature of the GA.

The individuals with low objective function values obtained after the final iteration represent the alternative pathways for obtaining the desired weld geometry. Table 3 lists the solutions, i.e. some of the many sets of welding variables. The solutions are spread over a range for all the three welding variables. The results show a variation of about 35% above the minimum value of power. Similarly, there is a variation of about 58% in speed and a significant variation, between -1.31 and 0.49 mm, in the defocus values among various combinations of solutions. Although the GA finds many solution sets, these solutions are not exhaustive and many more welding variable sets may exist for the same target geometry.

For each set of welding variables in table 3, the geometry calculated by the forward model was compared with the target geometry in figure 5. The calculated weld pool boundary is marked by the solidus temperature of the 5182 Al alloy.

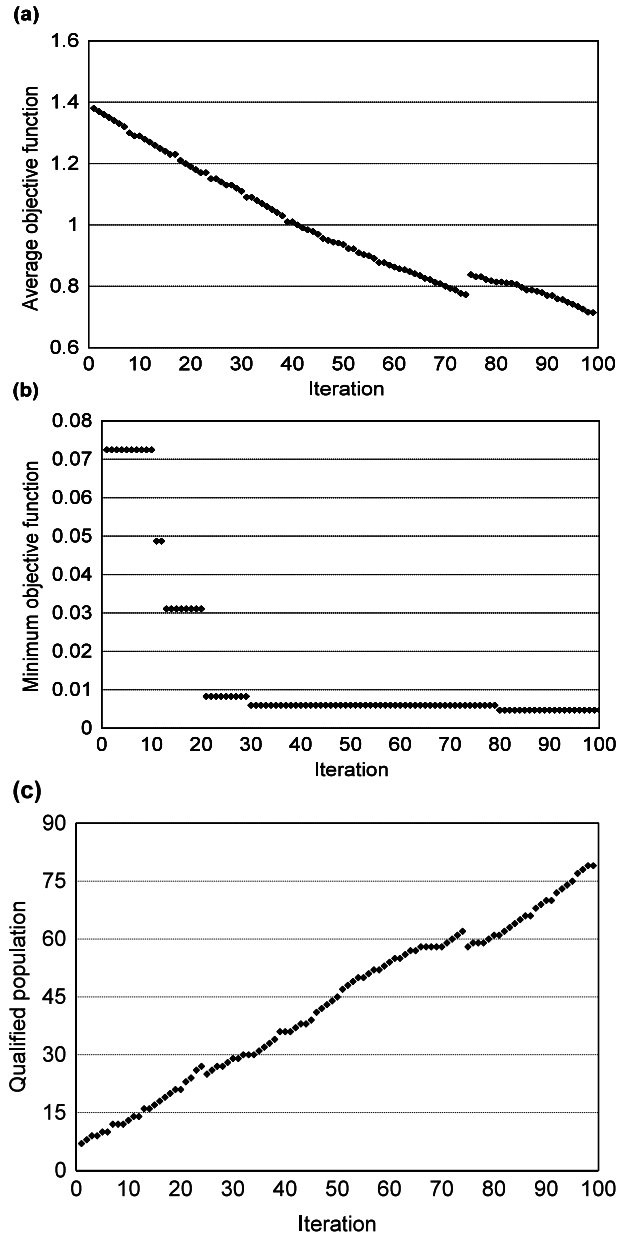


**Figure 4.** Plots show the (a) variation of population averaged objective function with iterations, (b) variation of minimum objective function value with iterations and (c) number of individuals whose objective function values defined by equation (12) are lower than 0.2.

**Table 3.** Optimized sets of welding variables, i.e. laser power, welding speed and beam defocus to achieve the following target weld pool dimensions: weld pool depth = 1.0 mm, weld pool width at the top of the plate = 1.63 mm and weld pool width at the bottom of the plate = 0.56 mm.

	Power (W)	Speed (mm s <sup>-1</sup> )	Defocus (mm)
(a)	2586	108	0.06
(b)	2843	157	-0.87
(c)	2947	133	0.34
(d)	3278	133	0.49
(e)	3354	162	0.22
(f)	3488	171	-1.31

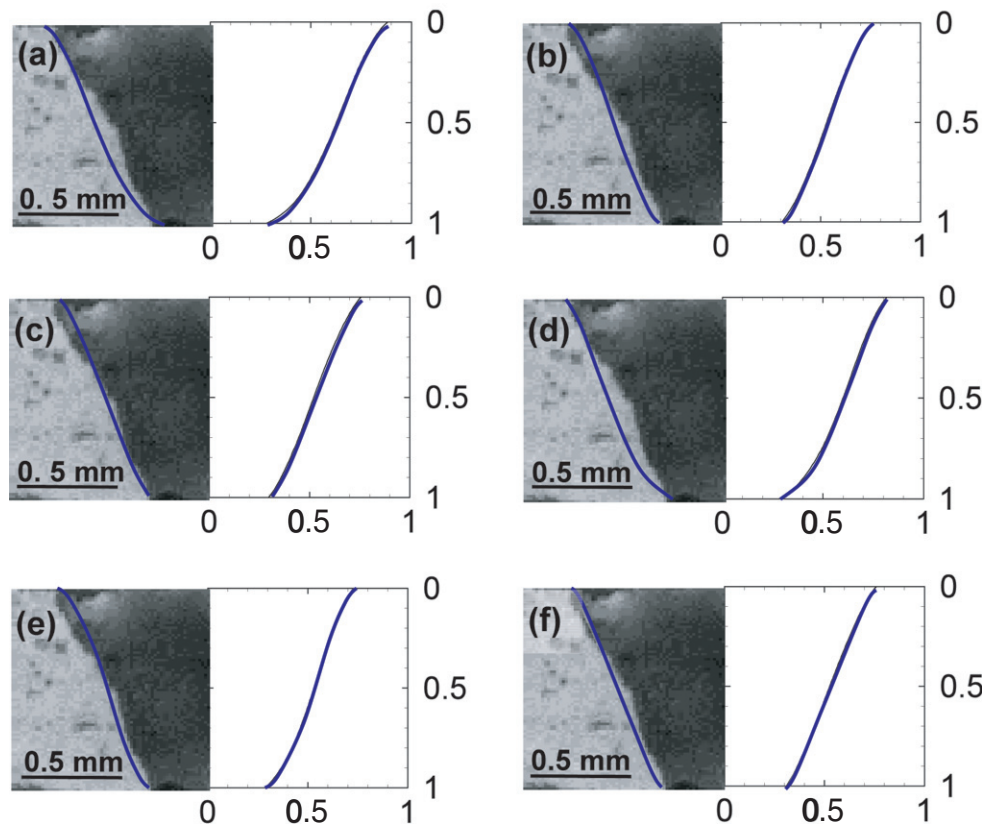


**Figure 5.** Comparisons between the calculated and the experimental weld pool geometry for different optimized combinations of welding variables given in table 3. The solid line marks the computed weld pool boundary which represents the equilibrium solidus temperature of the 5182 Al alloy.

The calculated geometry agreed reasonably well with the target geometry in each case as seen in figure 5. Thus, each set of welding variables listed in table 3 results in a weld geometry close to the target geometry. A higher welding speed may be desired if the production rate is an important consideration. On the other hand, system limitations may require use of a lower power laser. Note that the first set of welding conditions in table 3 is very close to the experimental welding conditions for our target geometry. Figure 6 shows the transverse section keyhole profile, along with the weld pool boundary, for each of the six solution sets of welding variables given in table 3. We see that very similar keyhole profiles and weld pools can be obtained for sets of welding variables very different from each other.

#### 4. Summary and conclusions

Numerical models of heat transfer can be combined with a GA and a limited volume of experimental data of weld geometry during keyhole mode laser welding to improve the reliability of predictions of temperature fields and weld geometry. A numerical heat transfer model and a real number-based GA were used for the estimation of optimized values of these uncertain parameters for the keyhole mode laser welding of the 5182 Al–Mg alloy. The weld pool geometry computed using the optimized values of two uncertain input parameters, laser beam absorption coefficient and beam radius at focal point,

was found to be in good agreement with the experimentally observed weld pool geometry.

For keyhole mode welding of the 5182 Al–Mg alloy the weld geometry can be tailored based on scientific principles via multiple pathways, i.e. using different combinations of laser power, welding speed and laser beam defocus. The GA was combined with the numerical heat transfer model of keyhole mode laser welding to find multiple sets of welding variables each of which could result in a specified weld geometry. Multiple sets of laser power, welding speed and beam defocus combinations with widely diverse values of these three parameters resulted in a given weld pool geometry. The predicted weld pool cross-sections were compared with the corresponding experimental values for each set of laser power, welding speed and beam defocus combinations. Although tailoring of weld geometry has been demonstrated in this paper, other weld attributes such as a desired cooling rate can also be achieved by the same methodology.

#### Acknowledgments

The work was supported by a grant from the US Department of Energy, Office of Basic Energy Sciences and Division of Materials Sciences, under grant number DE-FGO2-01ER45900. The authors thank Dr G G Roy, Mr R Nandan, Mr S Mishra and Mr A Kumar for their interest in this work.

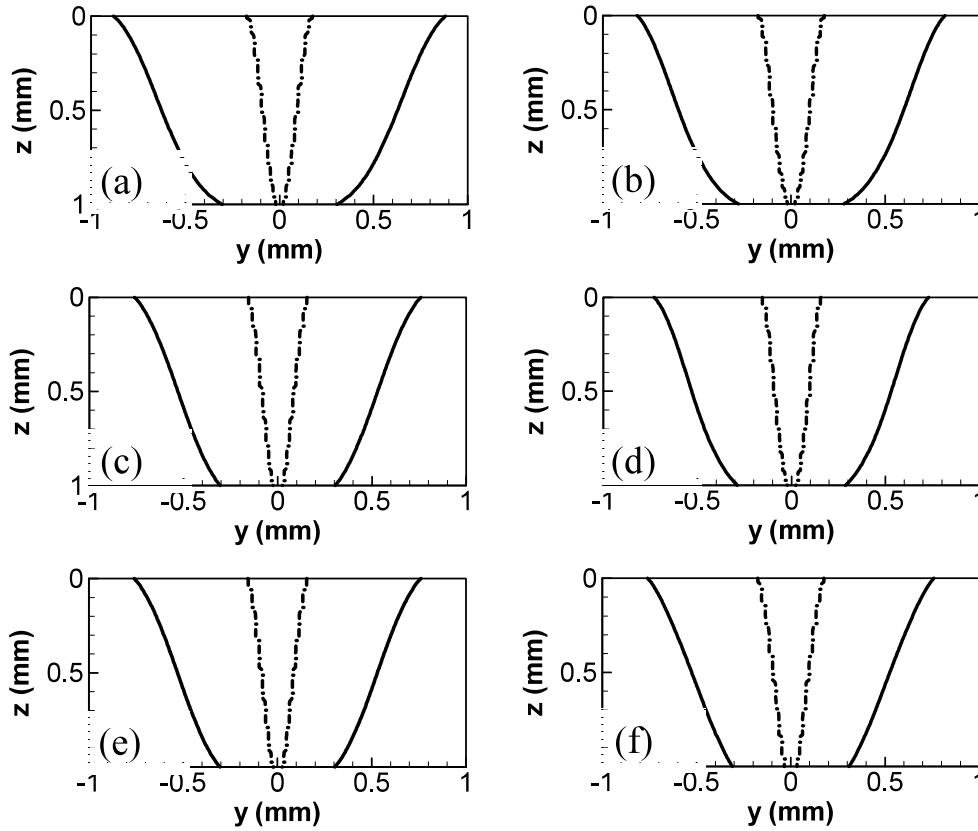


**Figure 6.** The transverse section keyhole boundary and the weld pool boundary for each of the six solution sets of welding variables in table 3. Broken lines mark the keyhole boundary and the solid lines indicate the weld pool boundary.

### Appendix. Parent-centric recombination (PCX)-based generalized generation gap (G3) genetic algorithm (GA)

The GA used in the present study to calculate the optimized values of the input variables is a PCX operator-based G3 model [28, 29]. This model was chosen because it has been shown to have a faster convergence rate on standard test functions as compared with other evolutionary algorithms. The algorithm for the model is as follows:

1. Each individual in a population represents a set of randomly chosen values of the two input variables, i.e. the beam radius at focus and the absorption coefficient. A parent refers to an individual in the current population. The best parent is the individual that has the best fitness, i.e. which gives the minimum value of the objective function, defined by equation (9), in the entire population. The best parent and two other randomly selected parents are chosen from the population.
2. From the three chosen parents, two new individuals are generated using a recombination scheme. PCX based G3 models are known to converge rapidly when three parents and two offspring are selected [29]. A recombination scheme is a process for creating new individuals from the parents.
3. Two new parents are randomly chosen from the current population.

4. A subpopulation of four individuals which includes the two randomly chosen parents in step 3 and two new offspring generated in step 2 is formed.
5. The two best solutions, i.e. the solutions having the least values of the objective function, are chosen from the subpopulation of four members created in step 4. These two individuals replace the two parents randomly chosen in step 3.
6. The calculations are repeated from step 1 again until convergence is achieved.

The above steps, as applied to the present study, are shown in figure 7. Every 25 iterations, all individuals forming a cluster near the best individual were replaced by randomly generated individuals to reduce any tendency of premature convergence of the population. The recombination scheme (step (2)) used in the present model is based on the PCX operator. A brief description of the PCX operator, as applied to the present problem of the three input variables, is described as follows.

First three parents, i.e.  $(f_1^0, f_2^0)$ ,  $(f_1^1, f_2^1)$ ,  $(f_1^2, f_2^2)$  are randomly selected from the current population. Here the superscripts denote the parent identification number. The mean vector or centroid,  $\vec{g} = ((f_1^0 + f_1^1 + f_1^2)/3, (f_2^0 + f_2^1 + f_2^2)/3)$ , of the three chosen parents is computed. To create an offspring, one of the parents, say  $\vec{x}^{(p)} = (f_1^0, f_2^0)$ , is chosen randomly. The direction vector,  $\vec{d}^{(p)} = \vec{x}^{(p)} - \vec{g}$ , is next calculated from the selected parent to the mean vector or centroid. Thereafter, from each of the other two parents,

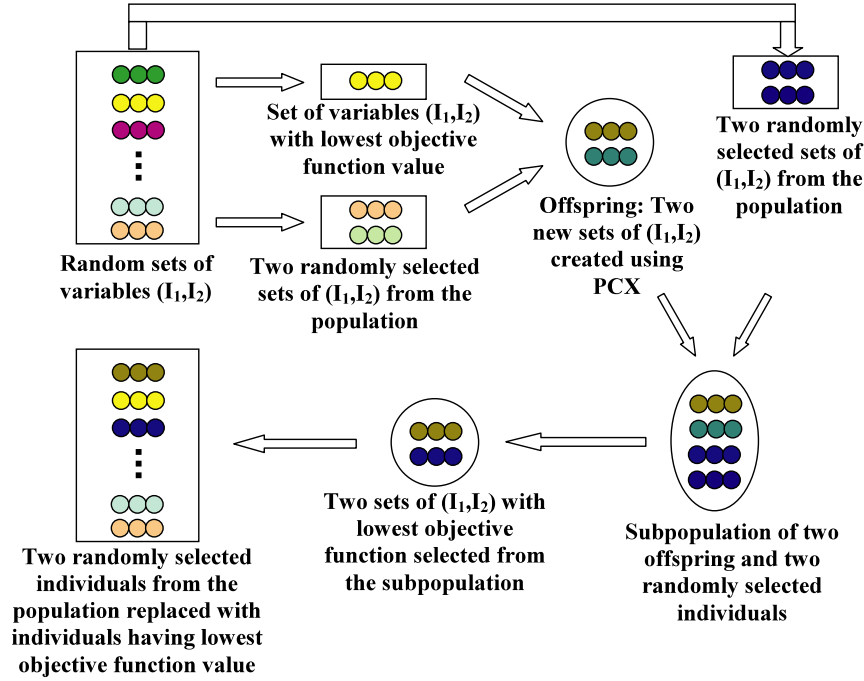


**Figure 7.** The G3 model using the PCX operator.

(This figure is in colour only in the electronic version)

i.e.  $(f_1^1, f_2^1)$  and  $(f_1^2, f_2^2)$ , perpendicular distances,  $D_i$ , to the direction vector,  $\vec{d}^{(p)}$ , are computed and their average,  $\bar{D}$ , is found. Finally, the offspring, i.e.  $\vec{y} = (f_1', f_2')$ , is created as follows:

$$\vec{y} = \vec{x}^{(p)} + w_\zeta |\vec{d}^{(p)}| + \sum_{i=1, i \neq p}^2 w_\eta \bar{D} \vec{h}^{(i)}, \quad (\text{A1})$$

where  $\vec{h}^{(i)}$  are the orthonormal bases that span the subspace perpendicular to  $\vec{d}^{(p)}$  and  $w_\zeta$  and  $w_\eta$  are randomly calculated zero-mean normally distributed variables. The values of the variables that characterize the offspring,  $\vec{y} = (f_1', f_2')$ , are calculated as follows:

$$f_1' = f_1^0 + f_{11} + f_{12}, \quad (\text{A2})$$

$$f_2' = f_2^0 + f_{21} + f_{22}, \quad (\text{A3})$$

where

$$f_{11} = w_\zeta \left( \frac{2f_1^0 - f_1^1 - f_1^2}{3} \right), \quad (\text{A4})$$

$$f_{21} = w_\zeta \left( \frac{2f_2^0 - f_2^1 - f_2^2}{3} \right), \quad (\text{A5})$$

$$f_{12} = w_\eta \left( \frac{a_2 + b_2}{2} \right) \left[ 1 - \left( \frac{2f_1^0 - f_1^1 - f_1^2}{3d} \right)^2 \right], \quad (\text{A6})$$

$$f_{22} = w_\eta \left( \frac{a_2 + b_2}{2} \right) \left[ 1 - \left( \frac{2f_2^0 - f_2^1 - f_2^2}{3d} \right)^2 \right]. \quad (\text{A7})$$

The expressions for the variables  $d$ ,  $a_2$  and  $b_2$ , used in equations (A6) and (A7), are as follows:

$$d = \sqrt{\left( \frac{2f_1^0 - f_1^1 - f_1^2}{3} \right)^2 + \left( \frac{2f_2^0 - f_2^1 - f_2^2}{3} \right)^2}, \quad (\text{A8})$$

$$a_2 = e_1 \times \sqrt{1 - (a_1)^2}, \quad (\text{A9})$$

$$b_2 = e_1 \times \sqrt{1 - (b_1)^2}, \quad (\text{A10})$$

$$a_1 = \sum_{i=1}^2 \frac{(f_1^1 - f_i^0)(2f_i^0 - f_1^1 - f_i^2)/3}{d \times e_1}, \quad (\text{A11})$$

$$e_1 = \sqrt{(f_1^1 - f_1^0)^2 + (f_2^1 - f_2^0)^2}, \quad (\text{A12})$$

$$b_1 = \sum_{i=1}^2 \frac{(f_2^1 - f_i^0)(2f_i^0 - f_1^1 - f_i^2)/3}{d \times e_2}, \quad (\text{A13})$$

$$e_2 = \sqrt{(f_1^2 - f_1^0)^2 + (f_2^2 - f_2^0)^2} \quad (\text{A14})$$

## References

- [1] He X, Elmer J and DebRoy T 2005 *J. Appl. Phys.* **97** 84909
- [2] He X, Fuerschbach P and DebRoy T 2004 *J. Appl. Phys.* **96** 4547
- [3] He X, Fuerschbach P and DebRoy T 2003 *J. Phys. D: Appl. Phys.* **36** 3079
- [4] He X, Fuerschbach P and DebRoy T 2003 *J. Phys. D: Appl. Phys.* **36** 1388
- [5] He X, Fuerschbach P and DebRoy T 2003 *J. Appl. Phys.* **94** 6949
- [6] Pitscheneder W, DebRoy T, Mundra K and Ebner R 1996 *Weld. J.* **75** 71s
- [7] Zhao H and DebRoy T 2001 *Metall. Trans. B* **32B** 163
- [8] Swift-Hook D E and Gick A E F 1973 *Weld. J.* **52** 492s

- [9] Andrews J G and Atthey D R 1976 *J. Phys. D: Appl. Phys.* **9** 2181
- [10] Klemens P G 1976 *J. Appl. Phys.* **47** 2165
- [11] Mazumder J and Steen W M 1980 *J. Appl. Phys.* **51** 941
- [12] Dowden J, Davis M and Kapadia P 1983 *J. Fluid Mech.* **135** 123
- [13] Dowden J, Postacioglu N, Davis M and Kapadia P 1987 *J. Phys. D: Appl. Phys.* **20** 36
- [14] Postacioglu N, Kapadia P, Davis M and Dowden J 1987 *J. Phys. D: Appl. Phys.* **20** 340
- [15] Mohanty P S and Majumder J 1997 *Sci. Technol. Weld. Joining* **2** 133
- [16] Kross J, Gratzke U and Simon G 1993 *J. Phys. D: Appl. Phys.* **26** 474
- [17] Sudnik W, Radaj D and Erofeev W 1996 *J. Phys. D: Appl. Phys.* **29** 2811
- [18] Metzbowser E A 1993 *Metall. Trans. B* **24** 875
- [19] Fujinaga S, Takenaka H, Narikiyo T, Katayama S and Matsunawa A 2000 *J. Phys. D: Appl. Phys.* **33** 492
- [20] Arata Y 1986 *Plasma, Electron and Laser Beam Technology* (Metals Park, OH: American Society for Metals)
- [21] Kaplan A 1994 *J. Phys. D: Appl. Phys.* **27** 1805
- [22] Zhao H and DebRoy T 2003 *J. Appl. Phys.* **93** 10089
- [23] Goldberg D E 1989 *Genetic Algorithm in Search, Optimization and Machine Learning* (Reading MA: Addison-Wesley)
- [24] Back T, Fogel D B and Michalewicz Z (ed) 2000 *Handbook of Evolutionary Computations* (New York: Oxford University Press; Bristol: Institute of Physics Publishing)
- [25] Mishra S and DebRoy T 2005 *J. Appl. Phys.* **98** 044902
- [26] Mishra S and DebRoy T 2005 *J. Phys. D: Appl. Phys.* **38** 2977
- [27] Kumar A and DebRoy T 2005 *Metall. Mater. Trans. A* **36** 2725
- [28] Deb K, Anand A and Joshi D 2002 *Evolutionary Comput.* **10** 371
- [29] Deb K 2001 *Multi-Objective Optimization Using Evolutionary Algorithms* 1st edn (New York: Wiley)
- [30] Rosenthal D 1946 *Trans. ASME* **48** 848
- [31] Block-Bolten A and Eagar T W 1984 *Metall. Trans. B* **15** 461
- [32] Collur M M, Paul A and DebRoy T 1987 *Metall. Trans. B* **18** 733
- [33] Sahoo P, Collur M M and DebRoy T 1988 *Metall. Trans. B* **19** 967
- [34] Kumar A, Mishra S, Elmer J W and DebRoy T 2005 *Metall. Mater. Trans. A* **36** 15
- [35] Pastor M, Zhao H, Martukanitz R P and DebRoy T 1999 *Weld. J.* **78** 207s
- [36] Bramson M A 1968 *Infrared Radiation: A Handbook for Applications* (New York: Plenum)